Mapping structures on the core–mantle boundary using Sdiff postcursors: Part II. Application to the Hawaiian ULVZ

Carl Martin, Thomas Bodin, Sanne Cottaar

To cite this version:

Carl Martin, Thomas Bodin, Sanne Cottaar. Mapping structures on the core–mantle boundary using Sdiff postcursors: Part II. Application to the Hawaiian ULVZ. Geophysical Journal International, 2023, 235, pp.2399 - 2409. 10.1093/gji/ggad345 . hal-04313019

Geophysical Journal International

Geophys. J. Int. (2023) **235,** 2399–2409 https://doi.org/10.1093/gji/ggad345
Advance Access publication 2023 September 7
GJI Seismology

Mapping structures on the core–mantle boundary using Sdiff postcursors: Part II. Application to the Hawaiian ULVZ

Carl Martin ,[1] Thomas Bodin [2] and Sanne Cottaar [1]

[1] *Bullard Laboratories, Department of Earth Sciences, University of Cambridge, CB3 0EZ, UK. E-mail: cm828@cam.ac.uk*
[2] *Laboratoire de Géologie de Lyon, UMR 5276, Université de Lyon, Villeurbanne, 69622, France*

Accepted 2023 September 4. Received 2023 August 10; in original form 2022 November 10

SUMMARY

We present a new data set of nearly 100 earthquakes which show clear evidence of the Hawaiian ultra-low velocity zone (ULVZ) in the S core-diffracted phase (Sdiff), representing the most comprehensive Sdiff data set of a ULVZ to date. Using a Bayesian inversion approach, as outlined in Martin *et al.*, and a subset of the data set, we characterise the 2-D morphology and velocity of the Hawaiian ULVZ. The results suggest that the ULVZ is smaller than previously estimated, with an elliptical shape, and oriented along the direction of the large low-shear velocity province boundary. Using forward modelling, we infer that the ULVZ has a height of 25 km and shear velocity reduction of 25 %.

Key words: Composition and structure of the mantle; Body waves; Computational seismology; Wave scattering and diffraction.

1 INTRODUCTION

The lowermost mantle is dominated by two large antipodal slow velocity structures—large low-shear velocity provinces (LLSVPs)—beneath Africa and the Pacific, which appear in all global tomographic models (e.g. Garnero *et al.* 2016). Sitting on the core–mantle boundary (CMB) lie smaller, but even more extreme reduced velocity (5–50 % dVs and 5–25 % dVp) features on the order of a few to tens of kilometres tall and up to 1000 km in lateral extent, dubbed ultra-low velocity zones (ULVZs, e.g. compilation by Yu & Garnero 2018). The largest of these, 'mega-ULVZs', have been identified near the Hawaii (Cottaar & Romanowicz 2012; J. Li *et al.* 2022, Z. Li *et al.* 2022), Samoa (Thorne *et al.* 2013, 2020; Krier *et al.* 2021), Iceland (Yuan & Romanowicz 2017), and Galapagos (Cottaar *et al.* 2022) hotspots, supporting a hypothesised spatial correlation to the LLSVP boundaries (Williams *et al.* 1998; Yu & Garnero 2018).

In this study, we collate and interrogate a data set of events which sample the Hawaiian ULVZ with the *S* core-diffracted phase (Sdiff). These waves diffract along the CMB and refract around ULVZs, resulting in 'postcursors' to the main phase (Sdiff+). Previous studies which have 3-D modelled mega-ULVZs using Sdiff phases have assumed a simplified uniform dVs cylindrical ULVZ in Hawaii (Cottaar & Romanowicz 2012; Z. Li *et al.* 2022), Iceland (Yuan & Romanowicz 2017) and Galapagos (Cottaar *et al.* 2022). These studies inferred axisymmetric structure by beamforming and backpropagating energy from the Sdiff+ arrivals at the seismic arrays, which showed that lensing had occurred. The simplest such structure that satisfies these observations is a cylinder. Furthermore, 3-D full waveform modelling up to the frequencies required for postcursors (0.1 Hz) is computationally expensive, taking 100–300 CPU hours per event per model. It is impractical therefore to do a rigorous grid search of potential 3-D morphological parameters. Using the wave front tracking software (Hauser *et al.* 2008; Martin *et al.* 2023), which runs on the order of a few CPU seconds, we are able to perform the first inversion for the shape of a ULVZ.

There is significant disagreement about the ULVZ landscape near the Hawaiian plume root other than that there is a patchwork of ULVZs (summarised in Fig. 1 and Table S1, Supporting Information). Despite studying a similar region, different phases, different filter bands and different approaches have led to different models.

Depending on its frequency, Sdiff will have sensitivity to different heights above the CMB: higher frequency waves have more sensitivity closer to the CMB but also a lower signal-to-noise ratio (SNR) due to weaker arrival amplitudes and stronger microseismic noise. Z. Li *et al.* (2022) investigated vertical stratification of a cylindrical model and the associated effects on this dispersive behaviour of postcursor waveforms in Hawaii, opting to relocate the preferred model of Cottaar & Romanowicz (2012) further SW but maintaining the 20 km height and −20 % dVs. The higher frequency waveforms were then interpreted to be sensitive to a ∼2 km thick basal layer with −40 % dVs. J. Li *et al.* (2022) also re-analysed the preferred model of Cottaar & Romanowicz (2012) with an augmented data set of S, ScS and Sdiff phases and extended the ULVZ footprint SW, but prefer a height of 50 km and −10 % dVs. Kim *et al.* (2020) propose instead that the observed postcursors can be equally well modelled by a cylinder ∼600 km tall and ∼450 km wide, which is interpreted as a deeply rooted plume conduit beneath the Hawaii hotspot, or a 50 km tall cylindrical ULVZ with otherwise the same parameters as the model proposed by Cottaar &

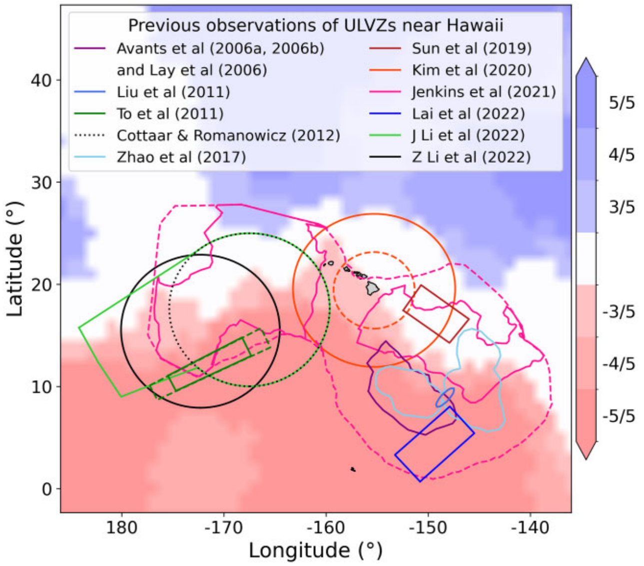

Figure 1. A map of ULVZ models associated with the Hawaiian plume and/or hotspot, compiled from studies using *S* phases (Avants *et al.* 2006a, b; Lay *et al.* 2006; Liu *et al.* 2011; To *et al.* 2011; Cottaar & Romanowicz 2012; Zhao *et al.* 2017; Sun *et al.* 2019; Kim *et al.* 2020; Jenkins *et al.* 2021; Lai *et al.* 2022; J. Li *et al.* 2022, Z. Li *et al.* 2022). The background model is a cluster analysis vote map from Cottaar & Lekic (2016), where positive (blue) represents number of models with fast velocities interpreted as slabs, and negative (red) represents number of models with slow velocities interpreted as LLSVPs. Solid and dotted lines are ULVZ models; dashed lines shown in the same colour represent alternative models proposed in the same study that both fit data equally well. The boundaries for Jenkins *et al.* (2021) have been taken as the 2.5 s (solid) and 1.0 s (dashed) contours of the pre/postcursor traveltimes, interpreted as thicker/stronger velocity reduction and thinner/weaker velocity reduction, respectively. A summary of the ULVZ models, including their velocity reductions and heights, is given in Table S1 (Supporting Information).

Romanowicz (2012). Similarly, To *et al.* (2011) prefer taller ULVZ models, 80 km or greater, with dVs at least 25 % reduced.

To the SE of Hawaii, several small patches of ULVZs have been identified which have been linked to the Hawaiian mantle plume (Avants *et al.* 2006a, b; Lay *et al.* 2006; Liu *et al.* 2011; Zhao *et al.* 2017; Sun *et al.* 2019; Jenkins *et al.* 2021; Lai *et al.* 2022), and potentially driven to the edge of the LLSVP by subducted slab motion (Lai *et al.* 2022). Using 2-D finite-difference synthetics with a combined data set of S, ScS and Sdiff phases, Lai *et al.* (2022) argue for a slab and plume model with a ULVZ embedded at the base of the plume modelled to be 30 km thick, ~300 km in lateral extent and −18 % dVs. Zhao *et al.* (2017) modelled the topography of the ULVZ near Hawaii using ScS, which was latterly expanded upon by Jenkins *et al.* (2021) to include the area also containing the Hawaiian mega-ULVZ mapped by Cottaar & Romanowicz (2012). Zhao *et al.* (2017) and Jenkins *et al.* (2021) both identify a regionally varying ULVZ topography, ranging from 0 to 20 km in height. Both studies require strong velocity anomalies, dVs 5–40 % reduced, but note that there is a strong trade-off between ULVZ height and velocity reduction. Additionally, Jenkins *et al.* (2021) interpret the mega-ULVZ to be 10–20 km thick, and no taller than 30 km, with dVs 15 % reduced. In contrast to these thinner models, Sun *et al.* (2019) identify a ULVZ in a similar region SE of Hawaii using ScS multipathing that is modelled to be 80 km tall, dVs 15 % reduced and ~150 km in lateral extent.

In this paper, we present a new data set of nearly 100 earthquakes which sample the Hawaiian ULVZ with Sdiff. It comprises data from the United States and Canada (including USArray in contiguous United States and Alaska), temporary arrays in Mexico and Central America, the Japanese F-net and networks in Australia and New Zealand. This represents the largest high-quality data set and broadest range of source–receiver geometries of any one particular ULVZ currently available in the literature, and offers great opportunities to study the properties of the Hawaiian mega-ULVZ, which are important in constraining its origin and role in mantle dynamics.

Whilst others have performed Bayesian inversions on ULVZ problems before (e.g. Thorne *et al.* 2020; Pachhai *et al.* 2022), we present the first lateral velocity map of a ULVZ from a Bayesian inversion. Using dynamic ray tracing software outlined in Hauser (2007) and Martin *et al.* (2023) to model wave fronts propagating across a spherical shell, we interrogate a subset of the new data set within a Bayesian inversion to estimate the morphology and velocity reduction of the Hawaiian ULVZ. Finally, we compare the 2-D inversion result with 3-D full waveform synthetics of a 3-D ULVZ model derived from the inversion.

This study is an application of the 2-D wave front tracker (2DWT) inversion methodology developed in the companion paper (Martin *et al.* 2023).

2 METHOD

2.1 Data

We have downloaded and inspected all earthquakes between 1990 and 2022 with magnitude 5.7+ at all depths from the Incorporated Research Institutions for Seismology (IRIS) catalogue. From this we have compiled a catalogue of nearly 100 high-quality events which sample the Hawaiian mega-ULVZ with Sdiff and/or the Sdiff depth phase (Table S2 and Fig. S1, Supporting Information). A small subset of these which give a broad range of source–receiver geometries, high number of stations and a high SNR are analysed in this study (Table 1 and Fig. 2).

Data were downloaded for stations 95 to 135° epicentral distance from the earthquake source, filtered between 10 to 20 s period, and then manually screened for SNR and presence of postcursor arrivals. The waveforms for these five events (Fig. 3) are aligned by the PREM Sdiff arrival time (Dziewonski & Anderson 1981) calculated using the TauP toolkit (Crotwell *et al.* 1999), and sorted by 1° bins of azimuth from source to receiver. The postcursors of Sdiff caused by the ULVZ, Sdiff+, are highlighted in their respective colours to guide the eye.

Event 3 has a prominent depth phase which cuts off the azimuth range that the postcursors can be constrained within, but postcursor observations still span a significant azimuth and epicentral distance range. For Event 4, the postcursor arrivals are significantly weaker in amplitude than the main arrivals, but can still be distinguished due to the SNR. The event shows postcursors extending to large off-axis angles. Event 5 is unique in that it has strong Sdiff+ postcursory energy but no Sdiff arrival; in this sense it differs from 3-D full waveform synthetics previously computed by Martin *et al.* (2023), which all feature a clear main arrival interfering with the postcursor energy, for example, in Events 1 and 2.

To extract the Sdiff+ arrival times, we correlate the waveforms with 1-D PREM synthetics calculated using Instaseis (van Driel

Table 1. Earthquake subset used in this study. All earthquake parameters are from the Global Centroid-Moment-Tensor project (Ekström *et al.* 1981). # is number of receivers with a positive postcursor detection. Source–receiver pairs have been extracted for positive postcursor observations.

Event	Date	Lon	Lat	Depth	Mag	#	Region
1	2005/08/08	140.23	−3.73	17.0	5.9	96	Irian Jaya, Indonesia
2	2006/03/14	127.31	−3.35	13.0	6.7	100	Seram, Indonesia
3	2008/08/30	147.49	−6.33	88.25	6.4	477	Eastern New Guinea Region, PNG
4	2015/01/23	168.36	−17.06	231.0	6.8	203	Vanuatu Islands
5	2016/09/08	158.47	−54.51	13.7	6.1	206	Macquarie Island Region
H	2010/03/20	152.33	−3.32	413.51	6.7	–	New Ireland Region, PNG

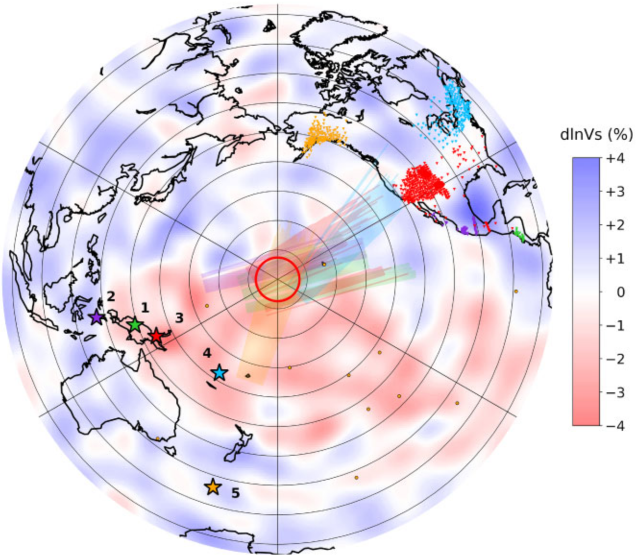

Figure 2. An equal area projection map centred on the ULVZ model (red circle) proposed by Z. Li *et al.* (2022). Five events and their Sdiff ray paths close to the CMB (2800 km and deeper) are shown in green (Event 1), purple (Event 2), red (Event 3), blue (Event 4) and orange (Event 5). The orange dots are surface hotspots. Each concentric ring represents 10° epicentral distance from the centre of the ULVZ model. The background model is the 2800 km depth slice of SEMUCB (French & Romanowicz 2014).

et al. 2015), again aligned with respect to the Sdiff arrival times calculated for Preliminary Reference Earth Model (PREM, Dziewonski & Anderson 1981). The arrivals are then picked as the continuous maxima of the correlation values. Further details and an example are available in Martin *et al.* (2023). Fig. 4 shows these arrival times plotted against the 'effective azimuth'. That is, the angle between the azimuth of source to ULVZ midpoint and the azimuth of ULVZ midpoint to receiver. This angle represents the degree of refraction of the postcursor. Then, if the ULVZ is axisymmetric, the postcursors should collapse onto a single parabola (Yuan & Romanowicz 2017; Martin *et al.* 2023); the success of this assumption suggests the ULVZ is indeed quasi-axisymmetric.

2.2 Null events and others not modelled

Sdiff waveforms can vary significantly, depending on the source-time function (e.g. complicated waveforms or poorly fitting CMT solutions), earthquake depth (e.g. interfering depth phases), energy directionality, azimuthal coverage (e.g. due to small seismic arrays) and level of SNR. As such, it was impractical to model a number of the earthquakes in our catalogue with the method introduced in the next section, which requires a distinguishable, separable postcursor to be able to pick the arrival from the data (Martin *et al.* 2023). This meant that a lot of the earthquakes which are in unique source–receiver geometries (e.g. Alaska and the west coast of contiguous USA; Figs S3 and S4a–b, Supporting Informtion) were unsuitable for modelling within our framework despite showing clear postcursory energy. These sorts of events would be suitable for 3-D full waveform tomographic modelling, if computational or algorithmic advances make such an inversion feasible.

Many of the earthquakes listed in the full catalogue would be appropriate for use within our inversion scheme, however there is still a computational cost associated with including additional data. We therefore only include the subset of five events as detailed in Table 1 in our analysis, selected for optimal coverage.

We do want to highlight a set of events that stood out during our data exploration: earthquakes from the Pacific Ridge, detected by the Japanese broadband F-net array, demonstrated consistently clear Sdiff arrivals but lacked Sdiff+ signals (Figs S4c–d, Supporting Information). This poses a significant challenge to our interpretation of the Hawaiian mega-ULVZ, which from all other source–receiver geometries that we have events for show clear postcursory energy. This possibly represents a 3-D topographical effect on the surface of the ULVZ, which might suggest a sloped top or velocity gradient into the LLSVP, but full waveform synthetic modelling of this effect is outside the scope of this study.

2.3 2DWT Bayesian inversion

A full description of the methodology (parametrisation, inversion formulation and convergence analysis), as well as its advantages and disadvantages, and various 2-D and 3-D synthetic tests can be found in Martin *et al.* (2023).

In short, we use the 2DWT from Hauser *et al.* (2008) and adapted by Martin *et al.* (2023) to model the postcursor arrival times of the ULVZ in the horizontal plane. Here, wave fronts are tracked across a spherical shell, which is 2-D in (θ, ϕ)-coordinate space. The postcursor traveltimes are computed for different ULVZ input velocity models. The scalar velocity field is parametrised as an ellipse (whose position, size, ellipticity and orientation can be varied) on a uniform background velocity, given by the PREM velocity at the CMB (7.2996 km s^{-1}, Dziewonski & Anderson 1981). The parameter space is defined so to be able to explore the parameter spaces of previous studies: location is within 15° of a chosen centre point (190°, 15°), velocity is 0.5–1.0 as a fraction of background velocity, semi-minor axis length is 50–800 km, rotation can take any value and eccentricity is up to 0.866.

The 2DWT forward model is implemented within a Bayesian inversion framework. After running the inversion for a while after convergence, a sparsely sampled distribution of velocity models is assumed to approximate the posterior distribution. From this, we use the inversion ensemble to produce estimates for the location, velocity reduction and lateral extent of the ULVZ, as well as their associated errors (Bodin *et al.* 2009).

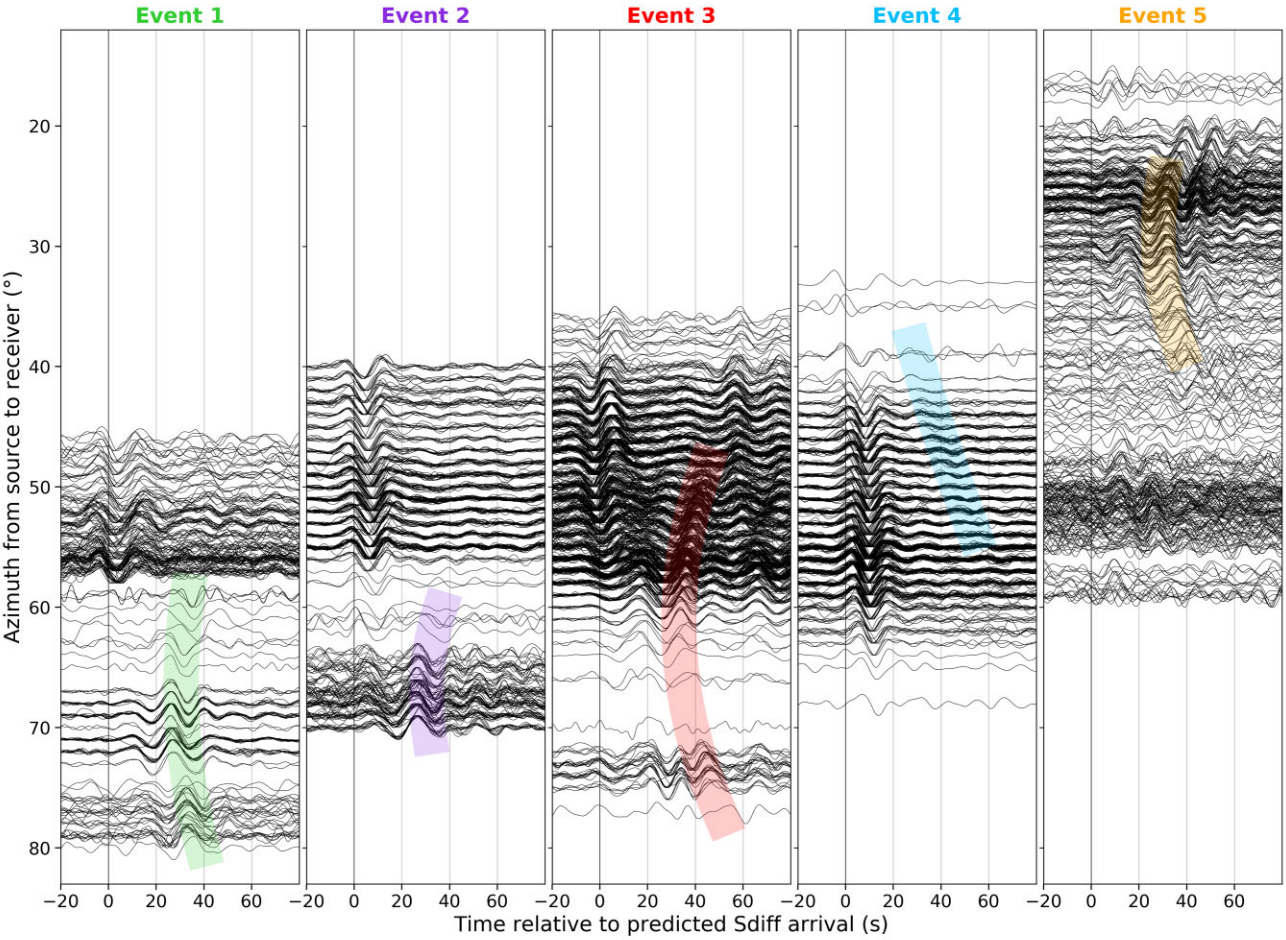

Figure 3. Waveforms for the selected five events which sample the Hawaiian mega-ULVZ; listed in Table 1 and source–receiver geometries shown in Fig. 2. Waveforms are sorted according to azimuth between source and receiver, and aligned with respect to predicted Sdiff arrival times from PREM (Dziewonski & Anderson 1981) calculated using the TauP toolkit (Crotwell *et al.* 1999). The postcursors have been highlighted in their respective colours to guide the eye. The arrival times extracted from these waveforms are shown in Fig. 4. This plot is reproduced without the postcursor highlights in Fig. S2 (Supporting Information).

We then estimate the sensitivity of our postcursors to the surrounding regions of the velocity map by allowing additional ellipses to be added to the equilibrium inversion ensemble. The inversion framework is then 'transdimensional' (Bodin *et al.* 2009; Galetti *et al.* 2017), that is, the number of ellipses in a velocity map is itself a variable.

2.4 3-D synthetic modelling using CSEM

From the ULVZ model obtained in the 2DWT inversion, we extend to 3-D full waveform synthetics with the use of the Coupled Spectral Element Method ('sandwiched'-CSEM; Capdeville *et al.* 2002, 2003; following Cottaar & Romanowicz 2012; Yuan & Romanowicz 2017; Cottaar *et al.* 2022). CSEM couples the normal mode summation for a 1-D Earth model with the spectral element solution for a full 3-D tomographic model in the lowermost 370 km of the mantle, allowing for computationally efficient 3-D full waveform synthetics calculated down to 10 s period. To do this, elliptic cylinders are injected into the whole mantle tomographic model SEMUCB (French & Romanowicz 2014). We then test a limited number of 3-D models due to computational expense; the chosen models are informed from the preferred 2-D inversion model and the height is based on estimates of the Sdiff+ frequency content (Martin *et al.* 2023).

3 RESULTS AND DISCUSSION

3.1 Inversion of real data

For the Sdiff+ arrivals extracted (Fig. 4) from the earthquake waveforms (Fig. 3), we perform a fully nonlinear Bayesian inversion with our 2DWT forward model for a single ellipse (Fig. 5a). The median map of the inversion ensemble shows an ellipse oriented SW-NE. We recover a characteristic ring of uncertainty in the standard deviation map of the inversion ensemble, indicating uncertainty in the boundary of the ULVZ (Galetti *et al.* 2017). This uncertainty is also readily visible in the velocity profile of the midpoint of the ULVZ (Fig. 6) and a SW-NE cross-section through the ensemble (Fig. 7). While the prior is a uniform distribution, the posterior distribution we recover is highly asymmetric: with a strong peak around −20 % velocity reduction, and a long tail skewed towards more extreme dVs. This is reflected in the cross-section: ensemble models with more velocity reduction have smaller ellipses, which is a consequence of the velocity-size trade-off (see discussion in Martin *et al.* 2023).

The overall parameters of the ellipse fitting the inversion data are taken to be the mean and standard deviation of the ensemble of ellipse parameters: an ellipse oriented at azimuth 56.9 ± 3.7° (approximately SW-NE), centred at (188.90 ± 0.42°, 16.15 ± 0.36°),

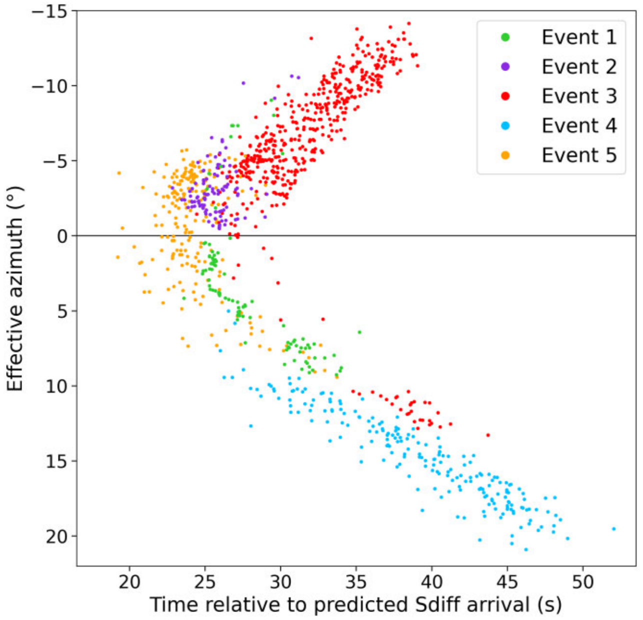

Figure 4. Extracted arrival times for the five events. The arrival times are plotted against the effective azimuth, which we define as the angle between the azimuth of source to an estimated ULVZ midpoint, and the azimuth of ULVZ midpoint to receiver.

with eccentricity 0.75 ± 0.05, semi-minor axis length 258 ± 44 km and dVs −21.7 ± 3.5 %.

To investigate the sensitivity Sdiff+ ray paths have to regions of the velocity map surrounding the ULVZ, we now permit creating and removing ellipses within the inversion—that is, we are now performing a transdimensional Bayesian inversion. We do this by continuing the inversion from the equilibriated endpoint of the initial ‘single-ellipse’ inversion (for details, see Martin *et al.* 2023). In this ‘multiple-ellipse’ inversion (Fig. 5b), we see two large ‘shadow zones’, which indicate regions of the velocity map which have little impact on the traveltimes calculated with the 2DWT and are therefore interpreted as regions of low sensitivity to the Sdiff+ ray paths. These shadow zones are located on the NW and SE due to the dominant SW-NE source–receiver geometry. There are two smaller shadow zones in front and behind the ULVZ, but which are distinctly separated from the ULVZ ring of uncertainty. Notably, in the median velocity map of the ensemble, we see two patches in the large shadow zones. Inspecting the NW-SE cross-section (Fig. 8) we see that in these shadow zones, the posterior is almost uniform: that is, the velocity field is not well resolved in these regions. We conclude that these are artefacts, and are indicative of the poor sensitivity Sdiff+ ray paths have to velocity variations in this region since the level of noise is comparable to the level of signal.

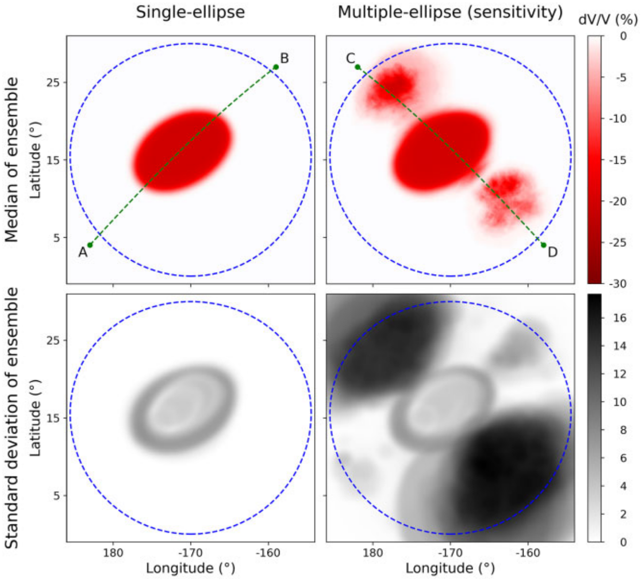

Figure 5. Median (upper) and standard deviation (lower) velocity maps of the ensemble of models of (left) single- and (right) multiple-ellipse inversions run for the arrivals in Fig. 4. The blue dashed line is the defined area of sensitivity on the velocity map. The cross-sections AB and CD are shown in Figs 7 and 8, respectively.

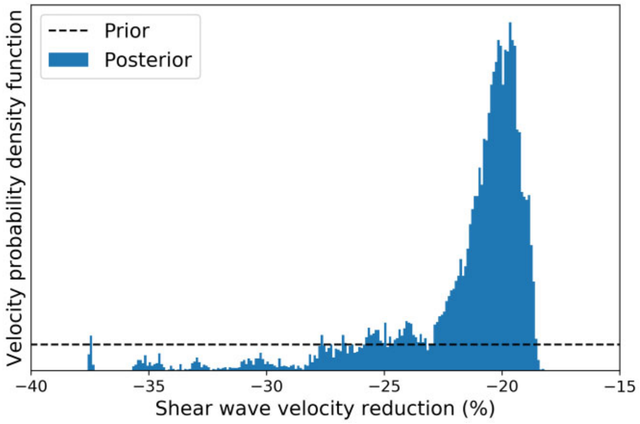

Figure 6. The probability density function of the dVs of the midpoint of the single-ellipse inversion ensemble from Fig. 5, representing the posterior distribution of the velocity of the Hawaiian mega-ULVZ. This is taken as the equilibrium distribution of the inversion once it has reached convergence (Fig. S5, Supporting Information).

Finally, we compute the arrival times for the median velocity map of the ensemble with the 2DWT, which show a good fit to the arrival times extracted from the waveform data (Fig. 9). Notably, the temporal shift in different events matches better than a circular ULVZ model (Fig. S6, Supporting Information).

3.2 Validation using 2DWT synthetics

We perform a series of validation tests using inversions with 2DWT synthetics to check how well we can resolve the parameters of the preferred ellipse—location, size, velocity reduction, orientation and ellipticity—with the source–receiver geometries available.

To test the location resolution we perform five inversions: one for the preferred elliptical ULVZ model, and then four shifted 100 km on the CMB in each of the NE, SE, SW and NW directions (Fig. S7, Supporting Information). Each inversion successfully recovers the input model with a high degree of accuracy, with the characteristic ring of uncertainty prominent in each. The results suggest we can resolve features successfully to within at least a location of 100 km by the present source–receiver geometry.

We then examine the trade-off between size and dVs (Fig. S8, Supporting Information). Here, we invert for a larger ellipse with a smaller velocity reduction and a smaller ellipse with a larger velocity reduction. Whilst all three inversions reproduce their respective input models, the smallest ellipse inversion produces an ensemble that is somewhat smeared. This can be seen more clearly when inspecting the velocity profiles of each of the inversion ensembles

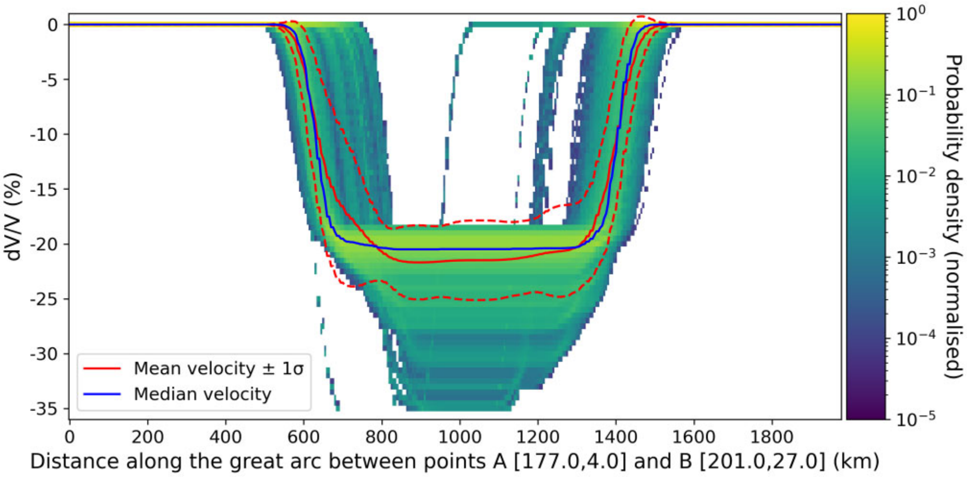

Figure 7. The probability density function of dVs of the AB cross-section of the ensemble of the single-ellipse inversion in Fig. 5. The mean (red) and median (blue) of the cross-sections are overlaid, with standard deviation marked in dashes.

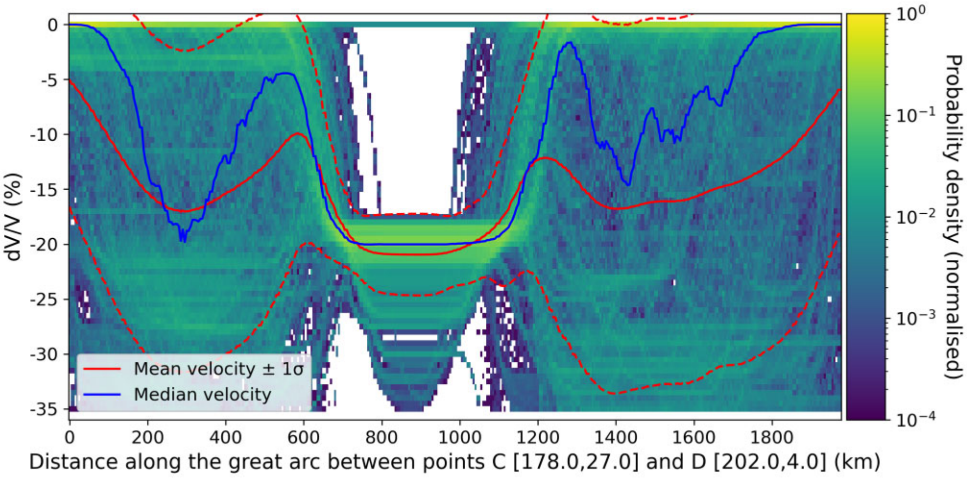

Figure 8. The probability density function of dVs of the CD cross-section of the ensemble of the multiple-ellipse inversion in Fig. 5. The mean (red) and median (blue) of the cross sections are overlaid, with standard deviation marked in dashes.

(Fig. S9, Supporting Information). The preferred and larger radius inversions produce Gaussian-like velocity distributions, albeit less reduced than their respective input models, whereas the smaller radius inversion results in a smeared bimodal distribution. This suggests that this size of anomaly is at the limit of resolution within our inversion methodology, as previously discussed in Martin *et al.* (2023).

The orientation of the ellipse model, SW-NE, is conspicuously in the predominant source–receiver geometry of the reference data (Fig. 2). We run inversions for the preferred ellipse model, rotated by 45°, 90° and 135° (Fig. S10, Supporting Information). It is notable that in the three rotated models, there is some residual SW-NE oriented models contributing to the ensemble, likely as a result of the overweighting in this orientation to the source–receiver geometries by the USArray. However, the overall rotation is recovered successfully in the median velocity map of the respective inversion ensembles (as well as their corresponding rings of uncertainty), which gives us confidence that this is a real effect and not just an artefact.

3.3 Re-modelling using 3-D synthetics

Martin *et al.* (2023) discussed some of the limitations of the 2DWT: primarily, the inability to capture 3-D mantle effects and the height of the ULVZ. Our results can be thought of as a velocity map for 10–20 s diffracted phases, similar to the phase velocity map produced for surface waves of a particular period (Galetti *et al.* 2017). This study also inverted for Sdiff+ arrivals extracted from 3-D full waveform synthetics calculated using CSEM (Capdeville *et al.* 2003) showing that the recovered velocity reduction was consistently less than the input model. We note that if the ULVZ is actually 20 km thick, then our recovered velocity is likely underestimated. If it is 50 km thick as some studies suggest (To *et al.* 2011; Kim *et al.* 2020; J. Li *et al.* 2022), then it is likely closer to the actual dVs value. As such, we now use our preferred elliptical ULVZ model (extracted from the median velocity map of the inversion ensemble) in CSEM, with a modified dVs −25 % and height of 25 km. We note that this is in agreement with the height inferred from analysis of frequency content of Sdiff+ waveforms (Cottaar & Romanowicz 2012; Z. Li *et al.* 2022) and within the range of

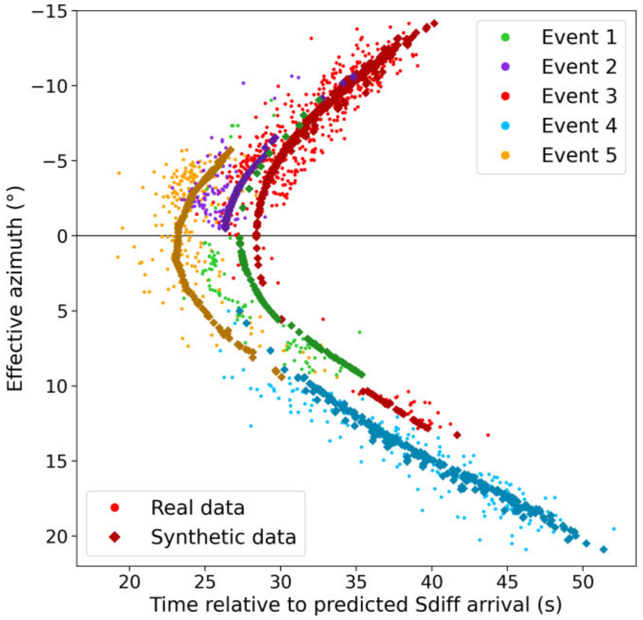

Figure 9. The arrival times for five events, as shown in Fig. 4. Overlain in darker colours are the arrivals calculated with the 2DWT for median velocity map of single-ellipse inversion.

permitted heights for the Hawaiian mega-ULVZ directly measured by a recent ScS study (Jenkins *et al.* 2021).

Fig. 10 shows the 3-D full waveform synthetics of the five events for the elliptical model with SEMUCB in the lowermost 370 km of the mantle (French & Romanowicz 2014). The highlighted regions track the Sdiff+ arrival times extracted from real data (as also plotted in Fig. 3), which indicates that Events 1–5 are well fitted by the elliptical model. It is noteworthy that the CMT solutions are not correct for our observed waveforms: particularly in Event 3, where there is a missing depth phase in the synthetics. For Event 5, the main phase is reduced in amplitude around the azimuths where the ULVZ is present, which is not captured by our model.

Whilst this model fits all the modelled Events 1–5, we are also able to test events that were not used in the inversion. Event H (Table 1) was a deep, high magnitude earthquake in Papua New Guinea with high-quality Sdiff+ arrivals detected by stations in the USArray, and has been used in several previous studies (Cottaar & Romanowicz 2012; J. Li *et al.* 2022, Z. Li *et al.* 2022). Fig. 11 shows the data and 3-D full waveform synthetics of several ULVZ models for this event. The cylindrical model of Z. Li *et al.* (2022) is larger than our elliptical model, but has a velocity reduction of 20 % and a height of 20 km. Our novel elliptical model appears to fit the waveform amplitude profile and Sdiff+ traveltime move out as well or better than the cylindrical ULVZ model. While differences might be minimal, it is noteworthy that the cylindrical ULVZ was mainly designed to fit this particular event (Cottaar & Romanowicz 2012; Z. Li *et al.* 2022) but this event is absent from our inversion data set. In the Supporting Information, we also compare our results against synthetics for further ULVZ models (J. Li *et al.* 2022; Kim *et al.* 2020). Several quantitative measures show that our preferred elliptical ULVZ model performs best and demonstrate the added value of our inversion framework over a purely forward modelling approach (Table S4, Supporting Information).

Figs S11 and S12 (Supporting Information) show 3-D full waveform synthetics for the additional events shown in Fig. S4 (Events 6–9, Table S3, Supporting Information), for the LLSVP and LLSVP with elliptical ULVZ, respectively. We note that the published CMT solutions do not capture much of the Sdiff/Sdiff+ waveform shape in Events 7–9, but the important thing is that we do not observe postcursory energy in these events caused by the Pacific LLSVP. The Sdiff depth phase in Event 6 shows significant curvature, which relates to the source–receiver distribution (stations further away from the source have a commensurately higher traveltime delay, which happens to resemble a postcursor moveout). The elliptical ULVZ synthetics show good agreement between the observed postcursors for earthquakes in Alaska and the West Coast, USA (Events 6 and 7), but there still remains the question why the Pacific Ridge earthquakes (Events 8 and 9) do not appear to sample the ULVZ as synthetically predicted.

Our inversion is based on the ‘absolute’ arrival time of postcursors, which are well fitted by our preferred elliptical model for event H (even though this event is not included in our data set). The main Sdiff arrival is sensitive to the velocities above the ULVZ and wavefront healing, both of which cannot be captured by the 2DWT. Thus, it is not possible to include this in our inversion approach. We note that there is information lost from the main phase, both in the delay time and in the damping of amplitude. Some have claimed other 3-D structures (To *et al.* 2016) or multipathing (To *et al.* 2011; Lai *et al.* 2022) are needed to explain more complex Sdiff waveforms. This study represents a step forward with the inclusion of the 2DWT within a Bayesian inversion, but better tomographic models of the lower mantle and further methodological and computational advancements will be required to address this inherently 3-D problem.

3.4 Relation of ULVZ model to Pacific LLSVP and other ULVZs

Previous studies have hypothesised a link between the locations of ULVZs and LLSVPs (e.g. Williams *et al.* 1998; Yu & Garnero 2018), and especially between mega-ULVZs and LLSVPs (e.g. Cottaar *et al.* 2022): Hawaii, Iceland, Galapagos and Samoa. 3-D modelling of the Hawaiian mega-ULVZ has, up until recently, been limited to cylindrical anomalies located close to the LLSVP boundary near Hawaii. Our results suggest that the ULVZ is elliptical, and lies parallel to the LLSVP boundary (Fig. 12). The preferred elliptical ULVZ model is plotted against the −0.5 % dVs contour of a number of whole mantle tomography models: SEMUCB (French & Romanowicz 2014), S40RTS (Ritsema *et al.* 2011), GLADM25 (Lei *et al.* 2020) and SP12RTS (Koelemeijer *et al.* 2016); in the background is a cluster vote map of fast and slow velocities by Cottaar & Lekic (2016). Each of these models has different sensitivities to the lowermost mantle, depending on-, for example, the data coverage and parametrisation used, but the overall correlation is invariant to the model: the ULVZ seems to lie parallel to the LLSVP boundary. This has consequences for the origin of the ULVZ and for geodynamic modelling of ULVZs. Our model is consistent with geodynamical models which show that ULVZs are pushed up against the edges of LLSVPs by slab-driven motion (e.g. M. Li *et al.* 2017, J. Li *et al*. 2022; Sun *et al.* 2019; Lai *et al.* 2022; Pachhai *et al.* 2022). This could suggest a resistive force provided by the LLSVP inducing an elliptical, rather than cylindrical, ULVZ structure. This may also be consistent with not being able to observe Sdiff+ from all source–receiver geometries, for example, from the Pacific Ridge towards Japan, which may correspond to a range of potential causes. For example, a smooth velocity gradient from the ULVZ into the

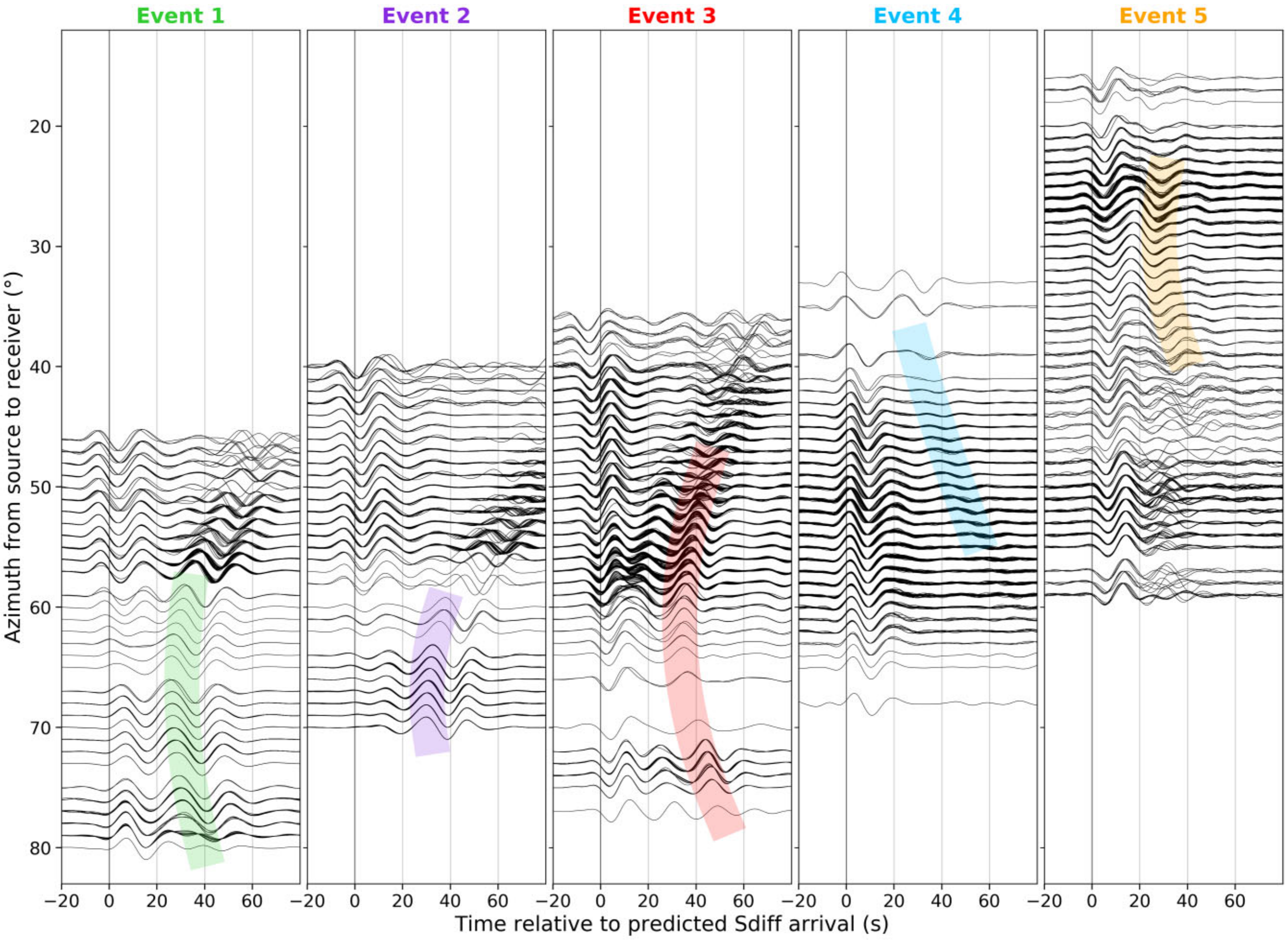

Figure 10. 3-D full waveform synthetics calculated using CSEM (Capdeville *et al.* 2003) for the selected five events with the preferred elliptical ULVZ model, with −25 % dVs and 25 km thickness; listed in Table 1 and source–receiver geometries shown in Fig. 2. Synthetic waveforms are sorted according to azimuth between source and receiver, and aligned with respect to predicted Sdiff arrival times from PREM (Dziewonski & Anderson 1981) calculated using the TauP toolkit (Crotwell *et al.* 1999). The highlights are smoothed azimuth-traveltime curves for Sdiff+ traveltimes picked from the real data (these are the same as in Fig. 3).

LLSVP, or a gentle downwards slope of the top of the ULVZ into the LLSVP.

Our preferred elliptical model with a dVs −25 % reduction and 25 km height is more reduced and taller than the cylindrical models by Cottaar & Romanowicz (2012) and Z. Li *et al.* (2022), but is only approximately half the area. This demonstrates the trade-off observed between velocity reduction, size and height. Our elliptical model is in direct contrast to J. Li *et al.* (2022) who recently proposed an increase in size of the Hawaiian ULVZ with a commensurate decrease in velocity reduction to −10 % and a height of 50 km; as well as others who argue for a taller ULVZ structure (e.g. To *et al.* 2011; Kim *et al.* 2020).

The Samoan mega-ULVZ, originally modelled by Thorne *et al.* (2013) and re-analysed by Thorne *et al.* (2020) and Krier *et al.* (2021), is unambiguously inside the Pacific LLSVP and is modelled to be ∼500 × 1600 km in lateral extent (Krier *et al.* 2021). This aspect ratio raises questions about nature of similarity between the elliptical Hawaiian and quasi-rectangular Samoan mega-ULVZs.

4 SUMMARY

We have presented the most comprehensive data set of events which sample the Hawaiian mega-ULVZ with Sdiff and related depth phases. Using a wave front tracking software on a 2-D spherical shell (2DWT), we perform a Bayesian inversion on a subset of our data set. The resulting inversion ensemble can be approximated by an ellipse centred at (188.90 ± 0.42°, 16.15 ± 0.36°), with a shear velocity reduction −21.7 ± 3.5 %, and oriented approximately SW-NE. Validation tests using our 2DWT forward model show that the preferred ULVZ model is robust against translation, rotation, and coupled variations in size and dVs with the real source–receiver distribution.

From this preferred 2-D elliptical model we infer and compute 3-D full waveform synthetics for a 3-D ULVZ model—an elliptic cylinder with the same elliptical shape as the preferred 2-D model, with a height of 25 km and velocity reduction of 25 %. This 3-D model performs comparatively to, if not better than, other models in the literature for an event not included in the 2DWT Sdiff+ data set.

Comparison with LLSVP boundaries from a number of whole mantle tomography models shows that the elliptical ULVZ model is oriented parallel with the LLSVP. This may have implications for the origins of the Hawaiian mega-ULVZ and its role in lower mantle dynamics, and therefore for considerations in geodynamic modelling.

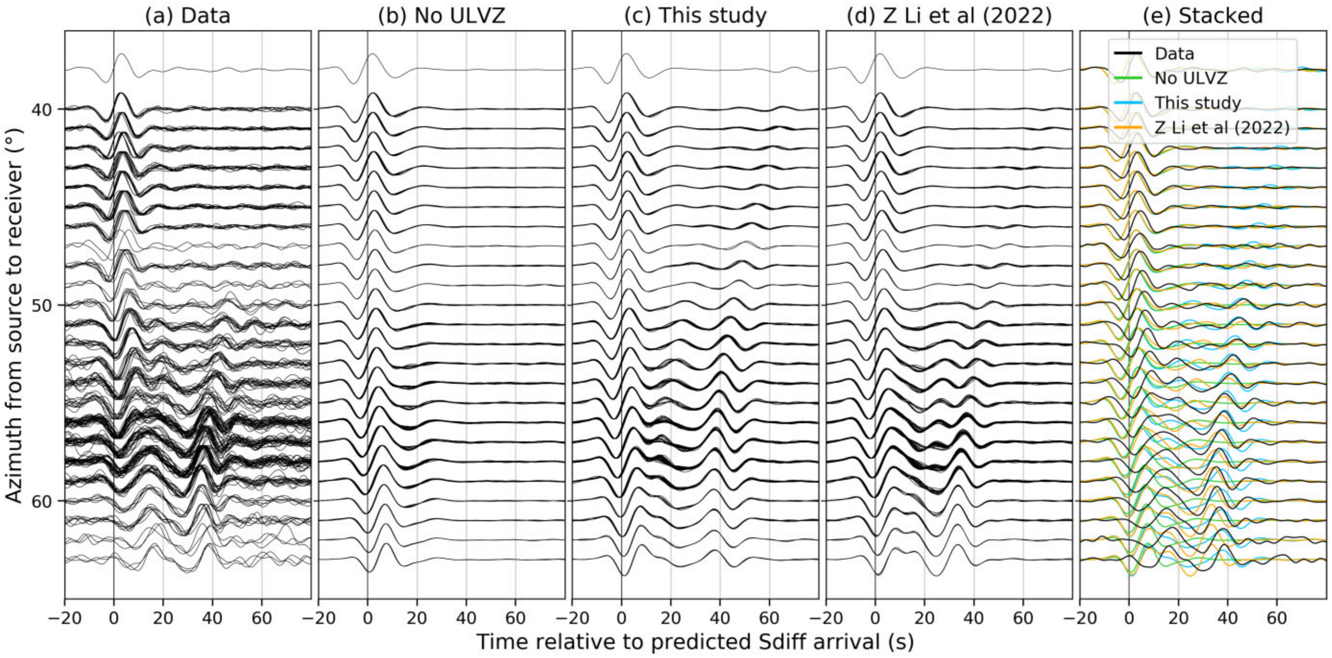

Figure 11. Data and synthetic waveforms for Event H detected by the USArray. This event is the one that ULVZ models from Cottaar & Romanowicz (2012) and Z. Li *et al.* (2022) are primarily fitted to. (a) Data filtered 10–20 s; 3-D full waveform synthetics for (b) the lowermost 370 km of SEMUCB (French & Romanowicz 2014) with no ULVZ, (c) SEMUCB with the preferred elliptical ULVZ model from this study, (d) SEMUCB with the preferred cylindrical ULVZ model from Z. Li *et al.* (2022) and (e) the linear stack data for (a–d). Data are binned into 1° azimuths.

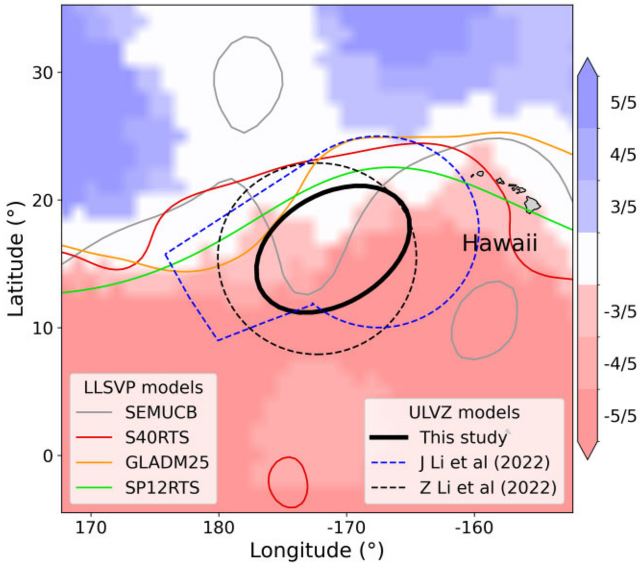

Figure 12. A comparison map of the elliptical ULVZ model with contours at $d\ln Vs$ of -0.5 % as an indication of the LLSVP boundary location in several whole mantle tomography models: SEMUCB (French & Romanowicz 2014), S40RTS (Ritsema *et al.* 2011), GLADM25 (Lei *et al.* 2020) and SP12RTS (Koelemeijer *et al.* 2016). The background model is a cluster analysis vote map from Cottaar & Lekic (2016), where positive (blue) represents number of models with fast velocities interpreted as slabs, and negative (red) represents number of models with slow velocities interpreted as LLSVPs. The preferred ULVZ models from Z. Li *et al.* (2022, dashed black) and J. Li *et al.* (2022, dashed blue) are overlaid.

DATA AND CODE AVAILABILITY

The facilities of IRIS Data Services (www.iris.edu), and specifically the IRIS Data Management Center, were used for access to waveforms and related metadata. IRIS Data Services are funded through the Seismological Facilities for the Advancement of Geoscience (SAGE) Award of the National Science Foundation under Cooperative Support Agreement EAR-1851048. Data from the TA network were made freely available as part of the EarthScope USArray facility, operated by IRIS and supported by the National Science Foundation, under Cooperative Agreements EAR-1261681. The facilities of NIED (http://www.bosai.go.gp/e/), and specifically the F-net (Okada *et al.* 2004), were used for access to waveforms and related metadata of Japanese seismometers. Earthquake parameters were used from the Global CMT Project www.globalcmt.org). Codes used will be made available by CM or SC upon request.

The waveform data used in this study are from the following networks: 6E (10.7914/SN/6E_2013), 7A (10.7914/SN/7A_2013), 7C (10.7914/SN/7C_2015), 7D (10.7914/SN/7D_2011), AG, AK (10.7914/SN/AK), AT (10.7914/SN/AT), AV (10.7914/SN/AV), AZ (10.7914/SN/AZ), BK (10.7932/BDSN), CC (10.7914/SN/CC), CI (10.7914/SN/CI), CN (10.7914/SN/CN), CO (10.7914/SN/CO), CU (10.7914/SN/CU), DK, EP, ET, G (10.18715/GEOSCOPE.G), GE (10.14470/TR560404), GS (10.7914/SN/GS), II (10.7914/SN/II), IM, IU (10.7914/SN/IU), IW (10.7914/SN/IW), KY (10.7914/SN/KY), LB, LD (10.7914/SN/LD), LI (10.7914/SN/LI), MB (10.7914/SN/MB), N4 (10.7914/SN/N4), NE (10.7914/SN/NE), NM, NN (10.7914/SN/NN), NR (10.7914/SN/NR), NU (10.7914/SN/NU), NV (10.7914/SN/NV), NW, NX (10.7914/SN/NX), NY (10.7914/SN/NY), OK (10.7914/SN/OK), OO (10.7914/SN/OO), PB, PE (10.7914/SN/PE), PO, PQ (10.7914/SN/PQ), RV (10.7914/SN/RV), SB (10.7914/SN/SB), SC, TA (10.7914/SN/TA), TD, TO (10.7909/C3RN35SP), UO (10.7914/SN/UO), US (10.7914/SN/US), UU (10.7914/SN/UU), UW (10.7914/SN/UW), WU, WY (10.7914/SN/WY), X4 (10.7914/SN/X4_2016), X7 (10.7914/SN/X7_2016), X8 (10.7914/SN/X8_2012), XC (10.7914/SN/XC_2006), XD (10.7914/SN/XD_2014), XE

(10.7914/SN/XE_2005), XF (10.7914/SN/XF_2006), XK (10.7914/SN/XK_2004), XL, XO (10.7914/SN/XO_2011), XP (10.7914/SN/XP_2008), XQ (10.7914/SN/XQ_2007), XR (10.7914/SN/XR_2008), XT, XU (10.7914/SN/XU_2006), XV (10.7914/SN/XV_2014), Y5, Y6, YC, YH (10.7914/SN/YH_2016), YM (10.7914/SN/YM_2013), YN (10.7914/SN/YN_2005), YO (10.7914/SN/YO_2003), ZA (10.7914/SN/ZA_2006), ZE (10.7914/SN/ZE_2015), ZG (10.7914/SN/ZG_2006), ZL (10.7914/SN/ZL_2011), ZQ (10.7914/SN/ZQ_2015), ZW (10.7914/SN/ZW_2013).

ACKNOWLEDGMENTS

This project has received funding from the European Research Council (ERC) under the European Union's Horizon 2020 research and innovation programme (grant agreement no. 804071—ZoomDeep). This work was performed using resources provided by the Cambridge Service for Data Driven Discovery (CSD3) operated by the University of Cambridge Research Computing Service (www.csd3.cam.ac.uk), provided by Dell EMC and Intel using Tier-2 funding from the Engineering and Physical Sciences Research Council (capital grant EP/T022159/1), and DIRAC funding from the Science and Technology Facilities Council (www.dirac.ac.uk). CM thanks Nick Rawlinson for sharing the 2DWT software with us, Florian Millet for technical assistance, and Jenny Jenkins, Pallav Kant and Adam Butler for helpful discussions. We would like to thank the Editor, Ebru Bozdag, and our reviewers (Jonathan Wolf, Daniel A Frost and another anonymous reviewer) for their comments which improved the quality of this manuscript. The authors declare that they have no competing interests.

SUPPORTING INFORMATION

Supplementary data are available at *GJI* online.

suppl_data

REFERENCES

Avants, M., Lay, T. & Garnero, E.J., 2006a. A new probe of ulvz s-wave velocity structure: Array stacking of scs waveforms, *Geophys. Res. Lett.,* **33**(7). https://doi.org/10.1029/2005GL024989.

Avants, M., Lay, T., Russell, S.A. & Garnero, E.J., 2006b. Shear velocity variation within the d region beneath the central pacific, *J. geophys. Res.: Solid Earth,* **111**(B5). https://doi.org/10.1029/2004JB003270.

Bodin, T., Sambridge, M. & Gallagher, K., 2009. A self-parametrizing partition model approach to tomographic inverse problems, *Inverse Probl.,* **15**(5). http://dx.doi.org/10.1088/0266-5611/25/5/055009.

Capdeville, Y., Larmat, C., Vilotte, J. & Montagner, J., 2002. A new coupled spectral element and modal solution method for global seismology: a first application to the scattering induced by a plume-like anomaly, *Geophys. Res. Lett.,* **29,** 32. https://doi.org/10.1029/2001GL013747.

Capdeville, Y., To, A. & Romanowicz, B., 2003. Coupling spectral elements and modes in a spherical Earth: an extension to the 'sandwich' case, *J. geophys. Int.,* **154**(1), 44–57.

Cottaar, S. & Lekic, V., 2016. Morphology of seismically slow lower-mantle structures, *Geophys. Suppl. Mon. Not. R. Astron. Soc.,* **207**(2), 1122–1136.

Cottaar, S. & Romanowicz, B., 2012. An unusually large ulvz at the base of the mantle near hawaii, *Earth planet. Sci. Lett.,* **355–356,** 213–222.

Cottaar, S., Martin, C., Li, Z. & Parai, R., 2022. The root to the Galápagos mantle plume on the core-mantle boundary, *J. geophys. Int.,* **195**(2), 1184–1195.

Crotwell, H., Owens, T. & Ritsema, J., 1999. The taup toolkit: flexible seismic travel-time and ray-path utilities, *Seismol. Res. Lett.,* **70,** 154–160.

Dziewonski, A. & Anderson, D., 1981. Preliminary reference earth model, *Phys. Earth planet. Inter.,* **25,** 297–356.

Ekström, G., Nettles, M. & Dziewoński, A., 2012. The global cmt project 2004–2010: 444 Centroid-moment tensors for 13,017 earthquakes, *Phys. Earth planet. Inter.,* **200,** 1–9.

French, S.W. & Romanowicz, B.A., 2014. Whole-mantle radially anisotropic shear velocity structure from spectral-element waveform tomography, *J. geophys. Int.,* **199**(3), 1303–1327.

Galetti, E., Curtis, A., Baptie, B., Jenkins, D. & Nicolson, H., 2017. Trans-dimensional love-wave tomography of the british isles and shear-velocity structure of the east irish sea basin from ambient-noise interferometry, *J. geophys. Int.,* **208**(1), 36–58.

Garnero, E., McNamara, A. & Shim, S.-H., 2016. Continent-sized anomalous zones with low seismic velocity at the base of earth's mantle, *Nat. Geosci.,* **9**(7), 481–489.

Hauser, J., 2007. *Multi Arrival Wavefront Tracking and Seismic Imaging,* PhD thesis, The Australian National University.

Hauser, J., Sambridge, M. & Rawlinson, N., 2008. Multiarrival wavefront tracking and its applications, *Geochem. Geophys. Geosyst.,* **9**. https://doi.org/10.1029/2008GC002069.

Jenkins, J., Mousavi, S., Li, Z. & Cottaar, S., 2021. A high-resolution map of hawaiian ulvz morphology from scs phases, *Earth planet. Sci. Lett.,* **563,** 116885. https://doi.org/10.1016/j.epsl.2021.116885.

Kim, D., Lekić, V., Ménard, B., Baron, D. & Taghizadeh-Popp, M., 2020. Sequencing seismograms: a panoptic view of scattering in the core-mantle boundary region, *Science,* **368**(6496), 1223–1228.

Koelemeijer, P., Ritsema, J., Deuss, A. & Van Heijst, H.-J., 2016. Sp12rts: a degree-12 model of shear-and compressional-wave velocity for earth's mantle, *J. geophys. Int.,* **204**(2), 1024–1039.

Krier, J., Thorne, M.S., Leng, K. & Nissen-Meyer, T., 2021. A compositional component to the samoa ultralow-velocity zone revealed through 2-and 3-d waveform modeling of sks and skks differential travel-times and amplitudes, *J. geophys. Res.: Solid Earth,* **126**(7), e2021JB021897. https://doi.org/10.1029/2021JB021897.

Lai, V.H., Helmberger, D.V., Dobrosavljevic, V.V., Wu, W., Sun, D., Jackson, J.M. & Gurnis, M., 2022. Strong ulvz and slab interaction at the northeastern edge of the pacific llsvp favors plume generation, *Geochem. Geophys. Geosyst.,* **23**(2), e2021GC010020. https://doi.org/10.1029/2021GC010020.

Lay, T., Hernlund, J., Garnero, E.J. & Thorne, M.S., 2006. A post-perovskite lens and d"heat flux beneath the central pacific, *Science,* **314**(5803), 1272–1276.

Lei, W. *et al.*, 2020. Global adjoint tomography-model glad-m25, *J. geophys. Int.,* **223**(1), 1–21.

Li, J., Sun, D. & Bower, D.J., 2022a. Slab control on the mega-sized north pacific ultra-low velocity zone, *Nat. Commun.,* **13**(1), 1–11.

Li, M., McNamara, A.K., Garnero, E.J. & Yu, S., 2017. Compositionally-distinct ultra-low velocity zones on earth's core-mantle boundary, *Nat. Commun.,* **8**(1), 1–9.

Li, Z., Leng, K., Jenkins, J. & Cottaar, S., 2022. Kilometer-scale structure on the core–mantle boundary near hawaii, *Nat. Commun.,* **13**(1), 1–8.

Liu, L., Tan, Y., Sun, D., Chen, M. & Helmberger, D., 2011. Trans-pacific whole mantle structure, *J. geophys. Res.: Solid Earth,* **116**(B4). https://doi.org/10.1029/2010JB007907.

Martin, C., Bodin, T. & Cottaar, S., 2023. Mapping structures on the core-mantle boundary using Sdiff postcursors: Part I. Method and validation, *J. geophys. Int.,* **X**(Y), Z. https://doi.org/10.1093/gji/ggad340.

Okada, Y., Kasahara, K., Hori, S., Obara, K., Sekiguchi, S., Fujiwara, H. & Yamamoto, A., 2004. Recent progress of seismic observation networks in japan—hi-net, f-net, k-net and kik-net—, *Earth Planets Space,* **56**(8), xv–xxviii.

Pachhai, S., Li, M., Thorne, M.S., Dettmer, J. & Tkalčić, H., 2022. Internal structure of ultralow-velocity zones consistent with origin from a basal magma ocean, *Nat. Geosci.,* **15**(1), 79–84.

Ritsema, J., Deuss, A., Van Heijst, H. & Woodhouse, J., 2011. S40rts: a degree-40 shear-velocity model for the mantle from new rayleigh wave dispersion, teleseismic traveltime and normal-mode splitting function measurements, *J. geophys. Int.,* **184**(3), 1223–1236.

Sun, D., Helmberger, D., Lai, V., Gurnis, M., Jackson, J. & Yang, H.-Y., 2019. Slab control on the northeastern edge of the mid-pacific llsvp near Hawaii, *Geophys. Res. Lett.,* **46**(6), 3142–3152.

Thorne, M., Garnero, E., Jahnke, G., Igel, H. & McNamara, A., 2013. Mega ultra low velocity zone and mantle flow, *Earth planet. Sci. Lett.,* **364,** 59–67.

Thorne, M.S., Pachhai, S., Leng, K., Wicks, J.K. & Nissen-Meyer, T., 2020. New candidate ultralow-velocity zone locations from highly anomalous spdks waveforms, *Minerals,* **10**(3), 211. https://doi.org/10.3390/min10030211.

To, A., Fukao, Y. & Tsuboi, S., 2011. Evidence for a thick and localized ultra low shear velocity zone at the base of the mantle beneath the central pacific, *Phys. Earth planet. Inter.,* **184**(3–4), 119–133.

To, A., Capdeville, Y. & Romanowicz, B., 2016. Anomalously low amplitude of s waves produced by the 3d structures in the lower mantle, *Phys. Earth planet. Inter.,* **256,** 26–36.

van Driel, M., Krischer, L., Stahler, S., Hosseini, K. & Nissen-Meyer, T., 2015. Instaseis: instant global seismograms based on a broadband waveform database, *Solid Earth,* **6,** 701–717.

Williams, Q., Revenaugh, J. & Garnero, E., 1998. A correlation between ultra-low basal velocities in the mantle and hot spots, *Science,* **281**(5376), 546–549.

Yu, S. & Garnero, E., 2018. Ultralow velocity zone locations: a global assessment, *Geochem. Geophys. Geosyst.,* **19**. https://doi.org/10.1002/2017GC007281.

Yuan, K. & Romanowicz, B., 2017. Seismic evidence for partial melting at the root of major hot spot plumes, *Science,* **357,** 393–397.

Zhao, C., Garnero, E.J., Li, M., McNamara, A. & Yu, S., 2017. Intermittent and lateral varying ulvz structure at the northeastern margin of the pacific llsvp, *J. geophys. Res.: Solid Earth,* **122**(2), 1198–1220.